Heterodimensional superlattice with in-plane anomalous Hall effect

Jiadong Zhou[1,3#], Wenjie Zhang[2#], Yung-Chang Lin[4#], Yao Zhou[5], Huifang Du[3], Bijun Tang[1], Jia Shi[6], Bingyan Jiang[2], Xun Cao[1], Bo Lin[1], Chao Zhu[1], Ya Deng[1], Qundong Fu[1], Ruihuan Duan[1], Xiaowei Wang[1], Jieqiong Chen[1], Shasha Guo[1], Wei Guo[3], Yizhong Huang[1], Yuan Yao[7], Yanfeng Gao[8], Yugui Yao[3], Kazu Suenaga[4,9]*, Xiaosong Wu[2]*, Zheng Liu[1,10,11]*

[1]School of Materials Science and Engineering, Nanyang Technological University, Singapore 639798, Singapore

[2]State Key Laboratory for Artificial Microstructure and Mesoscopic Physics, Frontiers Science Center for Nano-optoelectronics, and Collaborative Innovation Center of Quantum Matter, Peking University, Beijing 100871, China

[3]Key Lab of Advanced Optoelectronic Quantum Architecture and Measurement (MOE), Beijing Key Lab of Nanophotonics, and Ultrafine Optoelectronic Systems, and School of Physics, Beijing Institute of Technology, Beijing 100081, China

[4]Nanomaterials Research Institute, National Institute of Advanced Industrial Science and Technology (AIST), Tsukuba 305-8565, Japan

[5]School of Physical and Mathematical Sciences, Nanyang Technological University, Singapore, 637371, Singapore

[6]Department of Chemistry, National University of Singapore, 3 Science Drive 3, Singapore 117543

[7]Institute of Physics, Chinese Academy of Sciences, Beijing 100190, China

[8]School of Materials Science and Engineering, Shanghai University, Shanghai 200444, China

[9]The Institute of Scientific and Industrial Research, Osaka University, Osaka 567-0047, Japan

[10]CINTRA CNRS/NTU/THALES, UMI 3288, Research Techno Plaza, Singapore, Singapore

[11]School of Electrical and Electronic Engineering, Nanyang Technological University, Singapore, Singapore

Superlattices, a periodic stacking of two dimensional (2D) layers of two or more materials, offer a versatile scheme for material engineering so that new properties can be tailored. We report an intrinsic heterodimensional superlattice consisting of alternate 2D VS_2 and 1D VS chain array deposited directly by chemical vapor

deposition. This unique superlattice features an unconventional 1T stacking with a triclinic unit cell of 9 sets of VS_2/VS layers identified by scanning transmission electron microscopy. Surprisingly, an unexpected Hall effect, persisting up to 380 K, is observed when the magnetic field is in-plane, a condition under which the Hall effect usually vanishes. The magnetic field angular dependence of the effect indicates an exotic in-plane Ising-type spin anisotropy, resulting from the 1D VS chain. Our work breaks through the conventional understanding of superlattice and can stimulate the synthesis of more extraordinary super structures.

Superlattices have drawn intensive attention due to their intriguing electronic, optical, and magnetic properties that do not exist in intrinsic materials[1-5]. Generally, the traditional superlattices were formed among the materials with same dimension (such as 3D-3D, 2D-2D, and 1D-1D)[2,6-8]. Recently, the breakthroughs in 2D materials have enriched the superlattice families including van der Waals heterostructures (vdwHs), Moiré periodic patterns and the randomly intercalated compounds [9,10]. For instance, various typical superlattices such as the Moiré superlattices of hBN/graphene [11] and twisted graphene [12]), intermixing of $[(GeTe)_x/(Sb_2Te_3)_y]_n$ [13]and organic molecular (CTAB) intercalated black phosphorus (BP) [14] as well as the molecule-MoS_2 have been achieved [15]. Besides the mentioned above, the intercalated compounds including the Nb-based[16], V-based[17] and intrinsic 2D superlattice $MnBi_2Te_4$ [18]were reported. These superlattices possess the potential superconductivity[19] and ferromagnetism[20] for applications in quantum spintronic devices[21-23]. However, the superlattices were often

obtained via epitaxial growth or assembled by stacking 2D materials through different methods[6,24-27]. Meanwhile, in view of structures and dimensions, the reported superlattices belong to the 3D-3D, 2D-2D, and 1D-1D [6,16,17]. So far, the intrinsic heterodimensional superlattice formed between the intrinsic 2D (or 3D) and 1D has never been predicted and nor been realized in experiments.

Here, we report a new type of heterodimensional intrinsic superlattice structure in V-based 2D superlattice grown directly via a one-step CVD method. This superlattice is a periodic structure of 2D VS_2 layer and 1D VS chain layer, and 9 sets of VS_2/VS layers form a unit cell, belonging to space group of *P*1 with triclinic symmetry. Such structure has never been expected in the metallurgy. Due to the existence of 2D VS_2 and 1D VS array, the superlattice shows an intriguing room temperature in-plane anomalous Hall effect. The magnetic field angular dependence of the effect reveals an in-plane Ising-type spin anisotropy, complimentary to the celebrated out-of-plane one discovered in MoS_2 and $NbSe_2$[28,29]. The strong anisotropy stems from the 1D nature of the unique VS chain in the superlattice. Our work will open a new field towards heterodimensional superlattice for exploring excellent physical properties.

Note that the VS_2 and V_5S_8 can be easily obtained via CVD method[17,30]. In our experiment, the novel VS_2-VS superlattice was successfully achieved via controlling the growing conditions. Herein, a molten salt chemical vapor deposition (CVD) method was used to synthesize the V-based superlattices[30]. The corresponding setup is presented in Fig. S1. The growth method is depicted in Fig. 1a. By controlling the temperature of sulfur, at a high growth temperature with a short growth time (less than 2 min), VS_2-VS superlattice was achieved. While, at a low growth temperature (lower than 730 ^{o}C) with a long growth time (more than 3 min), VS_2 flakes were obtained (as

shown in Fig. S2). Figure1a also shows the optical image of VS_2-VS superlattice, which was synthesized with the precursor ratio of V_2O_5: KI larger than 5:1. It can be clearly seen in Fig. S3 that the VS_2-VS superlattice has a needle-like shape. At a low precursor ratio of 2:1, the superlattice array was obtained (see Fig. S3). This is attributed to the vapor-liquid-solid (VLS) growth mechanism[31]. Atomic force microscopy (AFM) measurements and more optical images are detailed in Fig. S3 and S4, respectively. Raman spectroscopy was performed to check the vibrational properties of VS_2-VS superlattice. Three main peaks located at 81 cm^{-1}, 336 cm^{-1} and 445 cm^{-1} were observed, as shown in Fig. 1b, which are fully different from the Raman spectra of VS_2[32]. We further measured optical second-harmonic generation (SHG) from thick samples and the wavelength of ~ 990 nm was selected as the excitation wavelength. The SHG signal clearly appears at 495nm (Fig. S5) indicating no inversion symmetry in crystal structure. The dependence of SHG intensity on the azimuthal angle shown in Fig. 1c illustrates the anisotropy of VS_2-VS superlattice. In order to further illustrate the valence state of V in the superlattice, XPS was conducted and the results are presented in Fig. 1d. We can clearly see that both V^{4+} and V^{2+} are co-existing in the superlattice, suggesting the formation of V-S bonding. The V*2p* peaks located at 525 eV and 517 eV are induced by oxidation of the samples. The corresponding XPS of S is detailed in Fig. S6. To assess the stability of VS_2-VS superlattices, the comparison of the stability between VS_2 and VS_2-VS superlattices is carried out via first principles calculations. The calculated Helmholtz free energies of VS_2-VS superlattices and VS_2 are shown in Fig. 1E, demonstrating that the VS_2-VS superlattices are stable below the 1500 K and naturally exist. The detailed calculations are presented in the methods part in Supplementary Materials.

To determine the atomic structure of as-synthesized superlattices, annular dark-field

scanning transmission electron microscopy (ADF-STEM) as well as the cross section TEM were performed. The grown material is a unique superlattice consisting of a periodic structure of 2D VS_2 and 1D VS chain array. Figure 2a shows the unit cell and the stacking structure of the VS_2-VS superlattice from the side view. Figure 2b shows the atomic model of the VS_2/VS superlattice from the top view. The VS_2 monolayers exhibit the 1T phase where the V and S atoms are arranged in octahedral coordination. The VS chains are 1D infinite array structure stacking between the VS_2 layers forming a large (1x3) surface unit cell, in which the V atoms are trigonal pyramid coordinated by S atoms. From the Fig. 2a and 2b, it clearly displays that the unit cell of the VS_2-VS superlattice is stacked in triclinic symmetry with 9 sets of VS_2/VS layers (blue dashed box in Fig. 2a). Note that the stacking order of the VS_2 layers is not conventional 1T stacking but a 3R (rhombohedral) stacking (indicated by gray dashed box in Fig. 2a) with the VS chain arrays intercalation. Figure 2c shows an annual dark field (ADF) image of the VS_2/VS superlattice cross section taken by using 60kV low-voltage STEM. The magnified ADF cross section image from the dashed rectangular in Fig. 2c is shown in Fig. 2d. The special stacking order matches the atomic model shown in Fig. 2a and 2b well. Some weak atomic contrasts appear in the interval of VS chains which should originate from part of the displaced VS chains.

Figure 3a displays colored low-mag ADF image of the superlattice from the top view, and the number of layers (labeled with circled numbers) can be distinguished by the contrast straightforwardly. Figure 3b shows an ADF image from the thinnest area. We found that the VS array layer is not stable when exposing to the surface (see also Fig. 2c and Fig. 3e) As a result, the thinnest stable structure is one VS array layer sandwiched by two layers of VS_2. The fast Fourier transform (FFT) image inserted in Fig. 3b reveals the structure information of the superlattice consisting of (1x1) hexagonal pattern and

(1x1/3) satellite spots derived for VS_2 layers and VS array layers, respectively. Furthermore, Fig. 3c and 3d display the magnified ADF images of the first and second thinnest VS_2/VS superlattice in the left panel, respectively. The corresponding simulation images in the right panel show excellent fit to the experimental images. More details about the structures of VS_2/VS superlattice are shown in Fig. S7.

We further performed electron energy loss spectroscopy (EELS) to investigate the charged state of the vanadium in the VS_2 and VS chains. Figure 3e shows an ADF image of the thinnest superlattice as $2VS_2$+1VS. At the up-right corner, one layer of VS_2 and VS chains were damaged by e-beam and left a monolayer VS_2. We performed an EELS line scan along the green line across seven VS chains. Figure 3f shows the 2D spectrum image with energy in the x axis and scan distance in the y axis. The cyan arrows point to the vanadium *L*-edges collected from pure VS_2, while the orange arrows point to the spectra which contain extra EEL signals from VS chains. Figure 3g shows the EEL spectra of VS_2+VS and VS_2 which are added up spectra from 7 orange arrows and 7 cyan arrows, respectively. The cyan spectrum represents the V^{4+} of VS_2, on the other hand, the orange spectrum contains an extra signal of V^{2+} of VS with redshift of *L*-edge and increasing in L_2 peak.

Due to the novel structure of the van der Waals superlattice formed by layered VS_2 and VS array, the superlattice displays a striking property, i.e., an unexpected Hall effect when a magnetic field is in the plane of the electric current and the Hall field. Figure 4a presents the field dependence of the Hall resistivity ρ_{xy} at 100 K for fields along three coordinate axes, x, y and z defined in Fig. 2. The current is in the y direction, while the transverse voltage along the x direction is measured. The z axis is perpendicular to the substrate. When B // z, the out-of-plane Hall effect (OPHE) is measured. When B is in

the xy plane, the Hall effect usually vanishes because of absence of the Lorentz force contribution, as is observed when B // y. The vanishing ρ_{xy} indicates a quite good alignment accuracy in our experimental setup. However, when B // x, there is a marked Hall effect that is even larger than OPHE, which immediately rules out the possibility of a perpendicular field contribution due to misalignment of the sample. From now on, we will call this unconventional effect the in-plane Hall effect (IPHE). It is worth pointing out that the effect should not be confused with the planar Hall effect, which is symmetric in B, as IPHE is a true Hall effect, in that it is anti-symmetric in B. Since the ordinary Hall cannot play a role under the current geometry, we believe that IPHE is a type of anomalous Hall effect (AHE) associated with spin-orbit coupling and the effect of the magnetic field is to introduce a Zeeman splitting to energy bands[33].

Unlike typical nonlinear anomalous Hall effect in ferromagnets, our IPHE is linear in field at all temperatures of measurements, which excludes any ferromagnetic order. Among all known vanadium sulfite compounds, only V_5S_8 and V_3S_4 exhibits an antiferromagnetic order below 32 K and 9 K, respectively[9,34]. The phase transition is manifested as a kink in the temperature dependent resistivity[35]. The resistivity of our superlattice remains smooth up to 380 K (see Fig. S8), showing no indication of a magnetic phase transition.

The observed IPHE is very robust, persisting up to 380 K, the highest temperature of our measurement apparatus. It decreases with temperature, as shown in Fig. 4b. Still, the Hall coefficient of IPHE at room temperature, 0.44×10^{-3} $cm^3\cdot C^{-1}$, is larger than that of OPHE (see Fig. S8 and S11 in Supplementary Materials II). The in-plane Hall conductivity is plotted as a function of temperature in Fig. 4c. Interestingly, it follows an exponential decay with T in the whole temperature range, which yields a gap $\Delta \sim 8$

meV. Since the intrinsic AHE is determined by the Berry curvature, which is strongly enhanced when two bands are close, known as hot-spots, this small gap is consistent with the large AHE observed.

It is well understood that the Berry curvature acts on electron like a magnetic field in momentum space and gives rise to the intrinsic AHE. Although the integral of the curvature over the Fermi sea is usually aligned with magnetization, it is not a requirement. In fact, it has been predicted that an in-plane magnetization can produce the quantum version of the AHE[36,37]. Our superlattice presents a rare case of an out-of-plane Berry curvature generated by an in-plane field. Although an ab initio calculation of the Berry curvature would be valuable for understanding the effect, it turned out to be an intimidating task, as the unit cell of the superlattice structure consists of 216 atoms in total. Nevertheless, the link between the particular superlattice structure and the unconventional property can be qualitatively uncovered to some extent by following the symmetry arguments in Ref. [36] and [38] (The detailed symmetry analysis can be found Supplementary Material). Basically, the mirror reflection perpendicular to the xy plane is incompatible with IPHE. Considering that magnetization is a pseudovector, an in-plane magnetization $\mathbf{m}_{\parallel}$ breaks any mirror symmetry in general and the Hall effect is allowed, except when $\mathbf{m}_{\parallel}$ is perpendicular to the mirror plane. Although our superlattice belongs to P1 space group, it is extremely close to C2/m, which has a mirror plane $\mathbf{M}_y$ perpendicular to the xy plane. When the magnetization is parallel to the y axis, $\mathbf{M}_y$ survives, resulting a zero Hall effect, which is in excellent agreement with our results. The symmetry analysis also provides a guideline for searching IPHE. For example, if there are two mirror planes perpendicular to each other in crystal, the system with an arbitrary in-plane $\mathbf{m}$ is invariant under a joint symmetry of $\mathbf{M}_x \otimes \mathbf{M}_y \otimes \mathbf{T}$,

where **T** represents time reversal symmetry. Consequently, the IPHE is forbidden.

We then map out the magnetic field angular dependence of the Hall effect, as shown in Fig. 4d to 4f. As the field is rotated in the zy plane, the Hall resistivity follows a sine function, consistent with a conventional Hall effect due to the out-of-plane field. In the case of the field being rotated in the xy plane, the Hall resistivity maximizes when B // x, while it vanishes when B // y, in good agreement with a simple sine function. When the field is rotated in the zx plane, the measured data is a sine function with a phase shift, which can be faithfully decomposed into IPHE and OPHE without any adjusting parameter (see the illustration in Fig. S9 of Supplementary Material). The fact that the angular dependence can be well described by simple trigonometric functions indicates that the IPHE is solely proportional to the projection of the field on the x axis. This result, though seemingly trivial, implies a highly unusual spin texture, that it, spins are aligned along the x axis. This unusual spin texture apparently results from the peculiar 1D VS chain of the superlattice, as it breaks the three-fold rotational symmetry of VS_2. Such an Ising-type spin anisotropy has been a hot topic, particularly associated with Ising superconductivity[28,29]. In stark contrast to the out-of-plane Ising-type spin anisotropy observed in MoS_2 and NbS_2, our superlattice displays an in-plane one, which may spark new ideas on spintronic devices.

In conclusion, we have synthesized the vertically stacked VS_2-VS superlattice via the CVD method. The Helmholtz free energy calculations demonstrated the stability of the superlattice. The STEM and cross-section TEM results have clearly revealed the atomic structure of VS_2-VS superlattice and demonstrated its unit cell contains 9 set VS_2/VS, which has not been obtained in V-based materials. The in-plane anomalous Hall effect at room temperature was first observed in the superlattice. The magnetic field angular

dependence reveals an astonishing in-plane Ising-type spin anisotropy, resulting from the 1D VS chain. Our results open a new avenue to synthesize superlattice and uncover the novel physical properties.

Supplementary Information is available in the online version of the paper

ACKNOWLEDGMENTS

This work was supported by the Ministry of Education, Singapore, under its MOE AcRF Tier 3 Award MOE2018-T3-1-002, MOE Tier 2 MOE2017-T2-2-136, Tier 3 MOE2018-T3-1-002. W.Z and X.W acknowledge the fund of the National Key Basic Research Program of China (No. 2020YFA0308800 and No. 2016YFA0300600) and NSFC (12074009 and No. 11774009). H.F.D., W.G. and Y.G.Y. acknowledge the fund of the National Key Basic Research Program of China (2017YFB0701603) and NSFC (No.51971037) and National Key R&D Program of China (Grant No. 2020YFA0308800). We also grateful for enlightening discussion with X. Dai and H. M. Weng and their preliminary attempts on ab initio calculations. Y.-C.L. and K.S. acknowledge to the JSPS-KAKENHI (JP16H06333), (18K14119), JST-CREST program (JPMJCR20B1, JMJCR20B5, JPMJCR1993), JSPS A3 Foresight Program, and Kazato Research Encouragement Prize. Y.F.G acknowledges the fund of the Innovation Program of Shanghai Municipal Education Commission (No. 2019-01-07-00-09-E00020), Shanghai Municipal Science and Technology Commission (18JC1412800).

Author contributions: J.Z, W.Z and Y.L contributed equally to this work. J.Z synthesized the superlattice and carried out the Raman and AFM measurements. Y.Z analyzed the XPS data. Y.Y carried out preliminary STEM experiments. Y.L and K.S

performed the STEM and EELS measurements. X.C and Y.H performed the FIB. W.Z, B. J and X.W carried out the device measurements. All authors contributed to the discussion of results.

Author Information Reprints and permissions information is available at www.nature.com/reprints. The authors declare no competing financial interests. Readers are welcome to comment on the online version of the paper. Correspondence and requests for materials should be addressed to Z.L (email: z.liu@ntu.edu.sg) or X.W (email: xswu@pku.edu.cn) or K. Suenaga. (email: ksuenaga.aist@gmail.com).

Methods

The superlattice was synthesized in a quartz tube with 1 inch in diameter. The length of the furnace is about 36 cm. The system of the reaction is shown in Fig. S1. Specifically, the alumina boat containing precursor powder was put in the center of the tube. The mixed powder (V_2O_5) and the salt （KI） with a ratio of 10:1 to 1:1 were used as precursors. Two SiO_2/Si substrates with 285 nm SiO_2 top layer were placed on the alumina boat with face to face and the mixed powder was put between the substrates. Another alumina boat containing S powder was put on the upstream of tube furnace at 200 ºC. The distance between the S boat and the precursor's boat is about 18 cm. Mixed gas of H_2/Ar with a flux gas (10/80 sccm) was used as the carrier gas. The heating rate of all reactions is 50 ºC/min. The growth temperature was 780 ~ 800 ºC and the growth time is 1 min to 5 min. The temperature was cooled down to room temperature naturally. All reaction materials were bought from Alfa Aesar with purity more than 99%.

STEM-EELS

STEM images were acquired by using ARM200F based UHV microscope equipped with a JEOL delta corrector and a cold field emission gun operating at 60 kV. The probe current is about 20 pA. The convergence semi-angle and the inner acquisition semi-angle are is 37 mrad and 76 mrad. Typical ADF images were taken with 1024 x 1024 pixels resolution by using 38.5 μs pixel time. The EELS core loss spectra were acquired

by using Gatan Rio CMOS camera optimized for low-voltage operation. EEL spectrum was acquired by using line scan with exposure time of 0.05 sec/pixel.

Data availability. The main data supporting the findings of this study are available within the article, and Supplementary Information. Extra data are available from the corresponding author upon request.

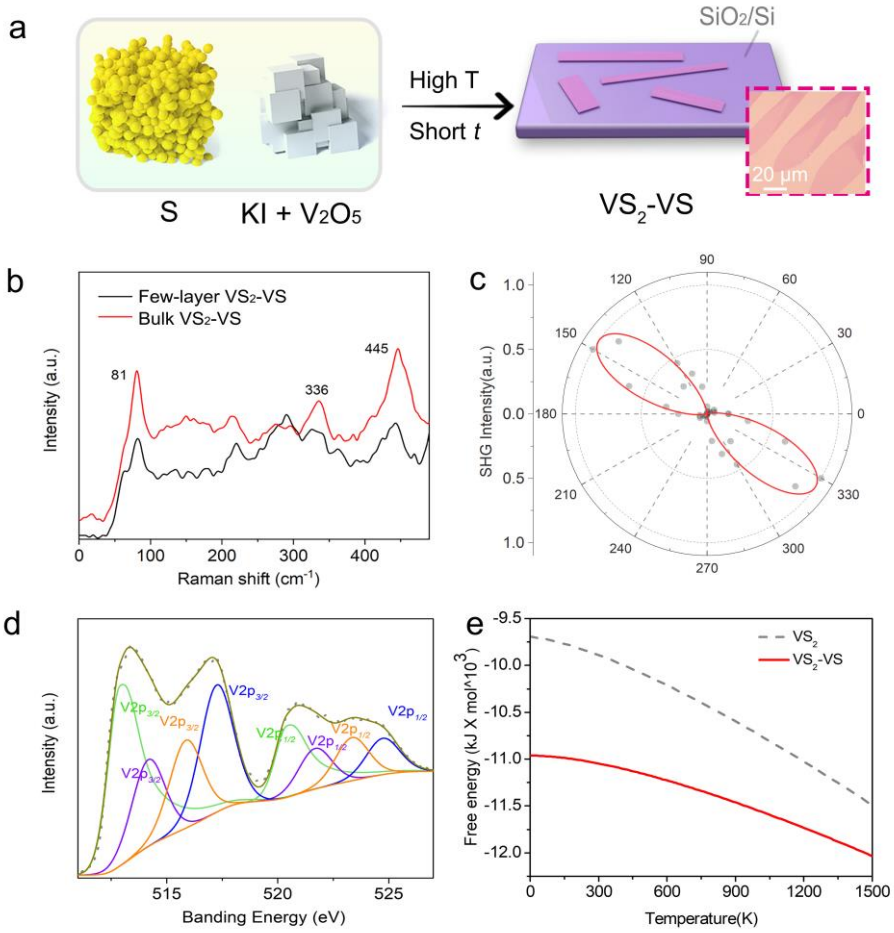

Figure | 1. Growth mechanism and optical images of VS_2-VS superlattice. (**a**) Growth mechanism of VS_2-VS. At a high temperature with a short growing time, VS_2-VS superlattice can be obtained. Figure 1a also shows the optical image of VS_2-VS superlattice flakes. (**b**) Raman spectra of VS_2-VS superlattice with different thickness.

(**c**) Azimuthal angle-dependence of SHG intensity in VS_2-VS, illustrating its anisotropic property. (**d**) XPS spectra of V*2p* in VS_2-VS superlattice. The V $2p_{1/2}$ and V $2p_{3/2}$ locating at 523 eV and 516 eV (orange curve) correspond to the V^{4+} in VS_2. The V $2p_{1/2}$ and V $2p_{3/2}$ siting at 521 eV and 514.5 eV are attributed to the V^{2+} in VS. The V $2p_{1/2}$ and V $2p_{3/2}$ siting at 520.3 eV and 513 eV highlighted by green curve are induced by the V element which have not reacted with S. While the V $2p_{1/2}$ and V $2p_{3/2}$ locating at high energy are attributed to the oxidized of superlattice, which also have been observed in the XPS spectra of S. (**e**) Helmholtz free energy of VS_2-VS superlattice and VS_2 under different temperature. The results show that the VS_2-VS superlattice is much more stable than VS_2 under the temperature below 1500 K, demonstrating the structure of superlattice is stable.

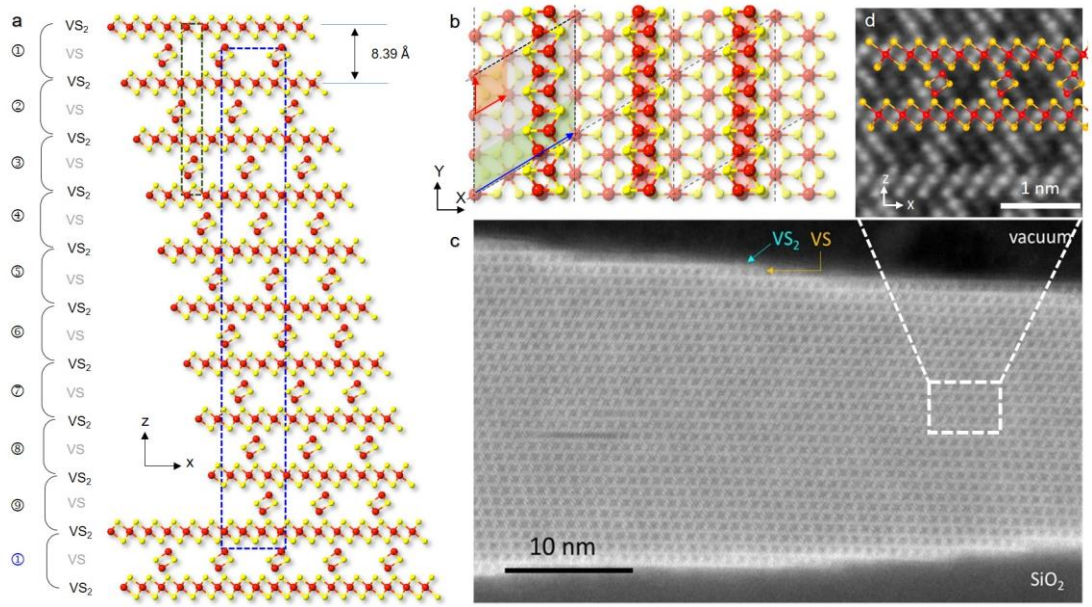

Figure | 2. Atomic structure of VS_2-VS superlattice. (a) The unit cell and the stacking structure of the VS_2-VS superlattice from side view. The crystal system is triclinic symmetry with space group of *P*1, where a=9.69Å, b=3.23Å, c=75.53Å, α=β=90°, γ=120°. **(b)** Atomic model of VS_2/VS superlattice from top view. Blue arrows indicate (1x1) unit cell of VS_2 lattice. Green arrows indicate the (1x3) unit cell of VS chain array.

Cyan and orange balls represent V and S atoms, respectively. **(c)** Cross section ADF image of VS_2-VS superlattice cut by focused ion beam. The surface is terminated in VS_2 layer. **(d)** The magnified ADF image from the white rectangular in (**c**).

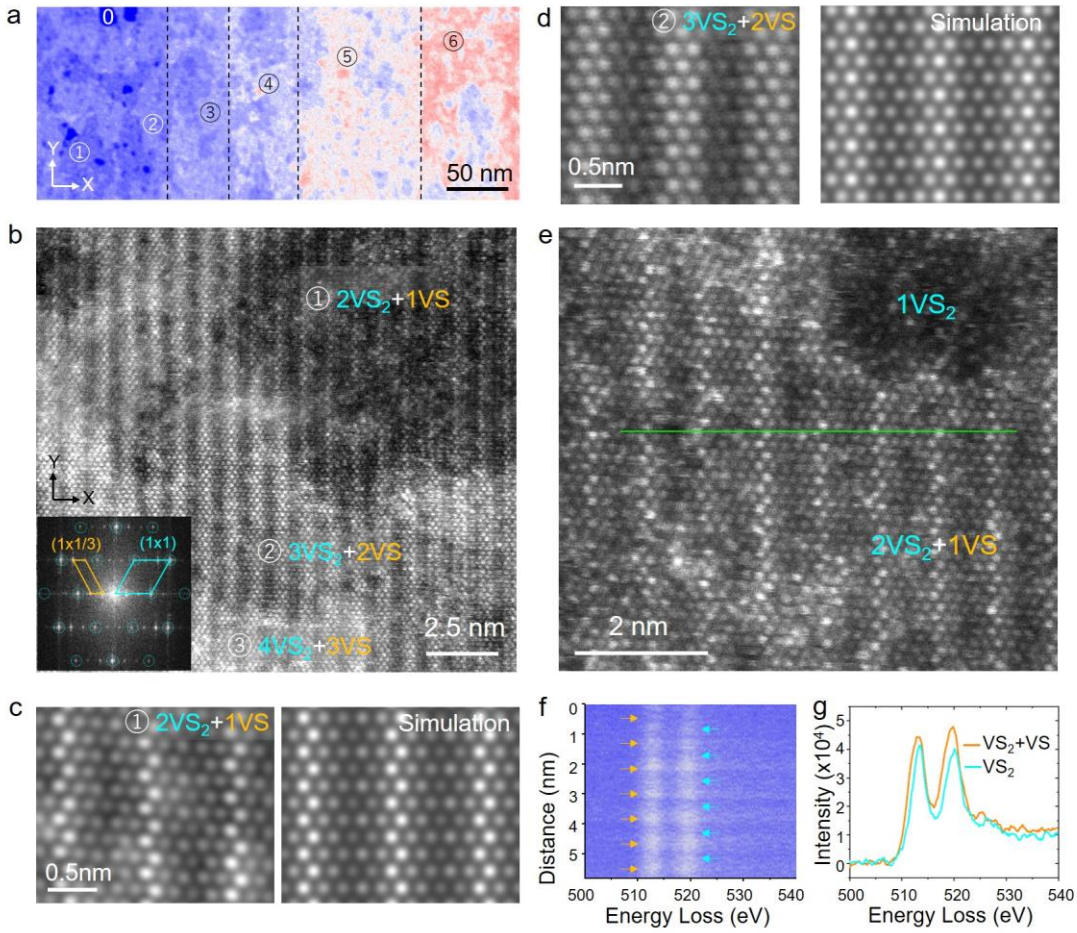

Figure | 3. Atomic structure of VS_2/VS superlattice. (a) A colored low-mag ADF image of the superlattice. The darkest contrast region marked with 0 is the vacuum. The different sets of superlattice layers are marked by circled numbers. **(b)** An atomic resolution ADF image of the superlattice at thin region. **(c**, **d)** Magnified ADF image and corresponding simulation image of the thinnest and second thinnest superlattices as $2VS_2$+1VS and $3VS_2$+2VS, respectively. **(e)** An ADF image of the $2VS_2$+1VS region with an area exposing monolayer VS_2. **(f)** EELS 2D spectrum image taken from a line scan along the green line in (**e**). Orange and cyan arrows point to the positions of

VS_2+VS and VS_2 regions, respectively. **(f)** EEL spectra of vanadium *L*-edge of VS_2+VS region (orange spectrum) and VS_2 region (cyan spectrum).

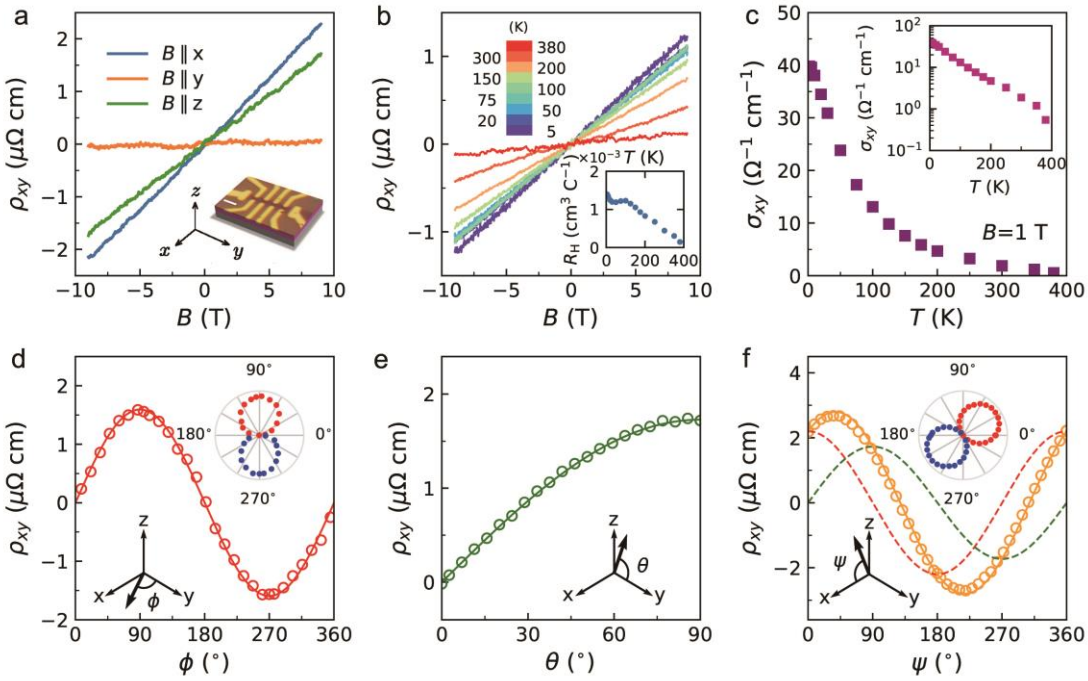

Figure | 4. Transport measurements of VS_2-VS superlattice. (**a**) Hall resistivity under magnetic field along different directions at T = 100 K. Since the magnetoresistance is negligible at this temperature (see the Supplementary Material), only a constant value needs to be subtracted from the raw data to get the Hall resistivity. The in-plane Hall (B // x) is even larger than the out-of-plane one (B // z). The inset is an illustration of the sample. The length of the scale bar is 2 μm. The current is along the y direction. (**b**) The IPHE at different temperatures. The inset is the temperature dependence of the Hall resistivity (**c**) The in-plane Hall conductivity versus temperature. The inset shows the same data plotted in a semi-log scale. (**d**), (**e**), and (**f**) Angular dependence of Hall resistivity at B = 9 T for a field in the xy, yz, xz-planes. Solid lines in (**d**) and (**e**) represent fits to sine functions. The data in (**f**) can be decomposed as the sum (solid yellow line) of the in-plane component (cosine, dashed red line) and the out-

of-plane component (sine, dashed green line). The insets in (**d**) and (**f**) show the angular dependence in a polar diagram. Red/blue color represent the positive/negative sign of the Hall resistivity, while the radius represents the absolute value. Data in **(d)** are measured at 5 K, while those in (**e**) and (**f**) are measured at 100 K. Date in (**a**), (**d**), (**e**), (**f**) are from one sample and data in (**b**) and (**c**) are from another sample.

References

1 Novoselov, K. S., Mishchenko, A., Carvalho, A. & Castro Neto, A. H. 2D materials and van der Waals heterostructures. *Science* **353**, aac9439 (2016).

2 Esaki, L. & Chang, L. L. New Transport Phenomenon in a Semiconductor "Superlattice". *Physical Review Letters* **33**, 495-498 (1974).

3 Liu, Y. *et al.* Van der Waals heterostructures and devices. *Nature Reviews Materials* **1,** 16042 (2016).

4 Björk, M. T. *et al.* One-dimensional Steeplechase for Electrons Realized. *Nano Letters* **2**, 87-89 (2002).

5 Dumestre, F., Chaudret, B., Amiens, C., Renaud, P. & Fejes, P. Superlattices of iron nanocubes synthesized from $Fe[N(SiMe_3)_2]_2$. *Science* **303**, 821-823 (2004).

6 Ryu, Y. K., Frisenda, R. & Castellanos-Gomez, A. Superlattices based on van der Waals 2D materials. *Chem Commun* **55**, 11498-11510 (2019).

7 Hu, M. & Poulikakos, D. Si/Ge superlattice nanowires with ultralow thermal conductivity. *Nano Lett* **12**, 5487-5494 (2012).

8 Davies, R. A., Kelly, M. J., Kerr, T. M., Hetherington, C. J. D. & Humphreys, C. J. Geometric and electronic structure of a semiconductor superlattice. *Nature* **317**, 418-419 (1985).

9 Silbernagel, B. G., Levy, R. B. & Gamble, F. R. Magnetic properties of V_5S_8: An NMR study. *Physical Review B* **11**, 4563-4570 (1975).

10 Jariwala, D., Marks, T. J. & Hersam, M. C. Mixed-dimensional van der Waals heterostructures. *Nat Mater* **16**, 170-181 (2017).

11 Yankowitz, M. *et al.* Emergence of superlattice Dirac points in graphene on hexagonal boron nitride. *Nature Physics* **8**, 382-386 (2012).

12 Cao, Y. *et al.* Unconventional superconductivity in magic-angle graphene superlattices. *Nature* **556**, 43-50 (2018).

13 Li, X.-B., Chen, N.-K., Wang, X.-P. & Sun, H.-B. Phase-Change Superlattice Materials toward Low Power Consumption and High Density Data Storage: Microscopic Picture, Working Principles, and Optimization. *Adv Funct Mater* **28,** 1803380 (2018).

14 Wang, C. *et al.* Monolayer atomic crystal molecular superlattices. *Nature* **555**, 231-236 (2018).

15 Zhong, Y. *et al.* Wafer-scale synthesis of monolayer two-dimensional porphyrin polymers for hybrid superlattices. *Science* **366**, 1379-1384 (2019).

16 Yang, J. *et al.* Ultrahigh-current-density niobium disulfide catalysts for hydrogen evolution. *Nat Mater* **18**, 1309-1314 (2019).
17 Ji, Q. *et al.* Metallic Vanadium Disulfide Nanosheets as a Platform Material for Multifunctional Electrode Applications. *Nano Lett* **17**, 4908-4916 (2017).
18 Deng, Y. *et al.* Quantum anomalous Hall effect in intrinsic magnetic topological insulator $MnBi_2Te_4$. *Science* **367**, 895-900 (2020).
19 Mitchson, G. *et al.* Structural Changes in 2D BiSe Bilayers as n Increases in $(BiSe)_{1+\delta}(NbSe_2)_n$ (n = 1-4) Heterostructures. *ACS Nano* **10**, 9489-9499 (2016).
20 Li, Z. *et al.* Molecule-Confined Engineering toward Superconductivity and Ferromagnetism in Two-Dimensional Superlattice. *J Am Chem Soc* **139**, 16398-16404 (2017).
21 Georgiou, T. *et al.* Vertical field-effect transistor based on graphene-WS_2 heterostructures for flexible and transparent electronics. *Nat Nanotechnol* **8**, 100-103 (2013).
22 Zhong, D. *et al.* Van der Waals engineering of ferromagnetic semiconductor heterostructures for spin and valleytronics. *Sci Adv* **3**, e1603113 (2017).
23 Hou, Y., Kim, J. & Wu, R. Magnetizing topological surface states of Bi_2Se_3 with a CrI3 monolayer. *Sci Adv* **5**, eaaw1874 (2019).
24 Geim, A. K. & Grigorieva, I. V. Van der Waals heterostructures. *Nature* **499**, 419-425 (2013).
25 Haigh, S. J. *et al.* Cross-sectional imaging of individual layers and buried interfaces of graphene-based heterostructures and superlattices. *Nat Mater* **11**, 764-767 (2012).
26 Chang, L. L. & Esaki, L. Semiconductor superlattices by MBE and their characterization. *Prog Cryst Growth Charact.* **2**, 3-14 (1979).
27 Yao, J. *et al.* Optical transmission enhancement through chemically tuned two-dimensional bismuth chalcogenide nanoplates. *Nat Commun* **5**, 5670 (2014).
28 Lu, J. M. *et al.* Evidence for two-dimensional Ising superconductivity in gated MoS_2. *Science* **350**, 1353-1357 (2015).
29 Xi, X. *et al.* Ising pairing in superconducting $NbSe_2$ atomic layers. *Nature Phys* **12**, 139-143 (2015).
30 Zhou, J. *et al.* A library of atomically thin metal chalcogenides. *Nature* **556**, 355-359 (2018).
31 Li, S. *et al.* Vapour-liquid-solid growth of monolayer MoS_2 nanoribbons. *Nat Mater* **17**, 535-542 (2018).
32 Yuan, J. *et al.* Facile Synthesis of Single Crystal Vanadium Disulfide Nanosheets by Chemical Vapor Deposition for Efficient Hydrogen Evolution Reaction. *Adv Mater* **27**, 5605-5609 (2015).
33 Polarization of local magnetic moments can also give rise to the anomalous Hall effect via skew scattering. The corresponding field dependence is expected to follow the Brillouin function, which sharply disagrees with the linear-B Hall observed down to 2 K. See Supplementary Material for more details.
34 De Vries, A. B. & Haas, C. Magnetic susceptibility and nuclear magnetic resonance of vanadium sulfides. *J Phys Chem Solids* **34**, 651-659 (1973).
35 Nozaki, H., Ishizawa, Y., Saeki, M. & Nakahira, M. Electrical properties of V_5S_8 single

crystals. *Physics Letters A* **54**, 29-30 (1975).
36 Liu, X., Hsu, H. C. & Liu, C. X. In-plane magnetization-induced quantum anomalous Hall effect. *Phys Rev Lett* **111**, 086802 (2013).
37 Liu, Z. *et al.* Intrinsic Quantum Anomalous Hall Effect with In-Plane Magnetization: Searching Rule and Material Prediction. *Phys Rev Lett* **121**, 246401 (2018).
38 Fang, C., Gilbert, M. J. & Bernevig, B. A. Bulk topological invariants in noninteracting point group symmetric insulators. *Physical Review B* **86** 115112 (2012).